



**HAL**  
open science

## NiMnCr layered double hydroxide-carbon spheres modified Ni foam: An efficient positive electrode for hybrid supercapacitors

Min Li, Ahmed Addad, Mathias Dolci, Pascal Roussel, Mu. Naushad, Sabine Szunerits, Rabah Boukherroub

### ► To cite this version:

Min Li, Ahmed Addad, Mathias Dolci, Pascal Roussel, Mu. Naushad, et al.. NiMnCr layered double hydroxide-carbon spheres modified Ni foam: An efficient positive electrode for hybrid supercapacitors. Chemical Engineering Journal, 2020, 396, pp.125370. 10.1016/j.cej.2020.125370 . hal-03089832

**HAL Id: hal-03089832**

**<https://hal.science/hal-03089832>**

Submitted on 23 Aug 2021

**HAL** is a multi-disciplinary open access archive for the deposit and dissemination of scientific research documents, whether they are published or not. The documents may come from teaching and research institutions in France or abroad, or from public or private research centers.

L'archive ouverte pluridisciplinaire **HAL**, est destinée au dépôt et à la diffusion de documents scientifiques de niveau recherche, publiés ou non, émanant des établissements d'enseignement et de recherche français ou étrangers, des laboratoires publics ou privés.

1 **NiMnCr Layered Double Hydroxide-Carbon Spheres Modified Ni Foam:**  
2  
3 **An Efficient Positive Electrode for Hybrid Supercapacitors**  
4  
5  
6  
7

8  
9 Min Li,<sup>1</sup> Ahmed Addad,<sup>2</sup> Mathias Dolci,<sup>1</sup> Pascal Roussel,<sup>3</sup> Mu. Naushad,<sup>4</sup> Sabine Szunerits<sup>1</sup>  
10  
11 and Rabah Boukherroub<sup>1\*</sup>  
12  
13  
14  
15  
16

17 <sup>1</sup>*Univ. Lille, CNRS, Centrale Lille, Univ. Polytechnique Hauts-de-France, UMR 8520 -*

18 *IEMN, F-59000 Lille, France*  
19

20 <sup>2</sup>*Univ. Lille, CNRS, UMR 8207 – UMET, F-59000 Lille, France*  
21  
22

23 <sup>3</sup>*Univ. Lille, CNRS, ENSCL, Centrale Lille, Univ. Artois, UMR8181, UCCS-Unité de Catalyse*  
24  
25

26 *et Chimie du Solide, Lille, F-59000, France*  
27  
28

29 <sup>4</sup>*Department of Chemistry, College of Science, Bld#5, King Saud University, Riyadh, Saudi*  
30  
31

32 *Arabia*  
33  
34  
35  
36  
37  
38  
39  
40  
41  
42  
43  
44  
45  
46  
47  
48  
49  
50  
51  
52  
53  
54

55 \*To whom correspondence should be addressed: Rabah Boukherroub  
56

57 [rabah.boukherroub@univ-lille.fr](mailto:rabah.boukherroub@univ-lille.fr); Tel: +333 62 53 17 24)  
58  
59  
60  
61

## Abstract

New electrode composite materials consisting of NiMnCr Layered Double Hydroxides (LDHs) coated on carbon spheres (CS) supported on nickel foam (NiMnCr LDHs@CS/NF) were synthesized using a two step hydrothermal process. The obtained binder-free NiMnCr LDHs@CS/NF composite was investigated as a positive electrode for supercapacitors and achieved a high specific capacity of  $569 \text{ C g}^{-1}$  at  $3 \text{ A g}^{-1}$ ; this value was  $\sim 6.5$  times that of CS/NF ( $87.9 \text{ C g}^{-1}$  at  $3 \text{ A g}^{-1}$ ) and  $\sim 3.3$  times that of NiMnCr LDHs/NF composite ( $173.2 \text{ C g}^{-1}$  at  $3 \text{ A g}^{-1}$ ). The NiMnCr LDHs@CS/NF composite retained  $\sim 76\%$  of its original capacity after 10000 cycles, much better than  $\sim 54\%$  achieved by NiMnCr LDHs/NF composite, suggesting good reversibility and stability. Furthermore, a hybrid supercapacitor was fabricated using NiMnCr LDHs@CS/NF as the positive electrode and FeOOH nanorods deposited on NF (FeOOH/NF) as the negative electrode. The hybrid supercapacitor displayed an energy density of  $48 \text{ Wh kg}^{-1}$  at a power density of  $402.7 \text{ W kg}^{-1}$ . A home-designed windmill device was successfully driven by the as-fabricated supercapacitor device for about 25 s. Additionally, two as-fabricated hybrid supercapacitor cells in series were used to light up a yellow LED and a red LED in parallel for  $\sim 111 \text{ s}$  and  $\sim 343 \text{ s}$ , respectively. Taken together, these results indicate that the developed electrodes hold a promising potential in energy storage application.

**Keywords:** NiMnCr LDHs; Carbon spheres; Nickel foam; Energy storage; Supercapacitors.

## 1. Introduction

Layered double hydroxides (LDHs),  $M^{2+}_{1-x}M^{3+}_x(OH)_2(A^{n-})_{x/n} \cdot mH_2O$ ,  $M^{2+}$  and  $M^{3+}$  correspond to ( $Ni^{2+}$ ,  $Co^{2+}$ ,  $Cu^{2+}$ ,  $Mg^{2+}$ ,  $Mn^{2+}$ ) and ( $Al^{3+}$ ,  $V^{3+}$ ,  $Fe^{3+}$ ,  $Cr^{3+}$ ) metal cations, respectively,  $A^{n-}$  represents the interlayer anion ( $NO_3^-$ ,  $CO_3^{2-}$ ,  $OH^-$ ),  $x = M^{3+}/(M^{2+} + M^{3+})$  is the surface charge [1, 2], have evoked great attraction on the basis of their well-defined and high redox activity, and environmentally friendly nature. They have been employed in several processes such as oxygen evolution reaction [3, 4], hydrogen evolution reaction [5], corrosion protection [6], hot coal gas desulfurization [7], supercapacitors [8, 9] and so on.

Among all the above mentioned applications, the development of high performance supercapacitors represents a very active area of research. In fact, as the energy crisis and environmental pollution caused by fossil fuels are becoming a very serious issue worldwide, supercapacitors have aroused widespread attention as energy storage devices [10-12]. It is universally acknowledged that supercapacitors possess unique advantages like superior reversibility, long cycle life, and high power density [13-17].

LDHs, as electrode materials for supercapacitors, are usually faced with the problem of low electrical conductivity, hindering their application for energy storage devices. Therefore, hybridization of LDHs with highly conducting materials, particularly carbon-based materials, is potentially an effective means to achieve high electrical conductivity of the electrodes. In this context, Hao *et al.* realized a hierarchical porous structure consisting of NiCo LDHs loaded onto flexible carbon nanotubes as a flexible supercapacitor, exhibiting a capacity of  $486.6 \text{ C g}^{-1}$  at  $0.1 \text{ A g}^{-1}$  [18]. Yin *et al.* demonstrated that CoNi-LDH array on graphene-based fiber could achieve a capacity of  $285 \text{ mC cm}^{-2}$  at  $0.25 \text{ mA cm}^{-2}$  [19]. Bandyopadhyay *et al.* prepared a

1 composite of graphitic carbon nitride and graphene/Ni-Al LDH for supercapacitors, generating  
2  
3 a capacity value of  $595 \text{ C g}^{-1}$  at  $1 \text{ A g}^{-1}$  [20]. Huang *et al.* synthesized NiMn LDH/rGO  
4  
5  
6 nanocomposite with a capacity of  $750 \text{ C g}^{-1}$  at  $1 \text{ A g}^{-1}$  [21]. Even though, LDHs-based  
7  
8  
9 supercapacitors are described in the literature, there are many opportunities for designing  
10  
11 efficient electrode materials for supercapacitors based on LDHs, given the plethora of  
12  
13 combinations of  $M^{2+}/M^{3+}$  offered by these materials. Owing to its plentiful oxidation degrees  
14  
15 (+1 to +6), Cr was chosen as the third metal in LDHs with the aim to enhance the intrinsic  
16  
17 activity and performance of LDHs electrodes in supercapacitors.  
18  
19  
20

21  
22  
23 Additionally, supercapacitors are still not applied on a large scale because of their relatively  
24  
25 low energy density ( $E$ ). Given that  $E$  is related to the capacity ( $C$ ) and the operation potential  
26  
27 window ( $\Delta V$ ) according to  $E=0.5C \Delta V^2$ , the fabrication of hybrid supercapacitors represents  
28  
29 an effective means to enlarge the operation potential window. Generally, carbon materials  
30  
31 (activated carbon [22], carbon nanotubes [23], graphene [24] *etc.*) are applied as the negative  
32  
33 electrodes for hybrid supercapacitors owing to their large working potential window and  
34  
35 stability. However, designing new suitable and cost effective negative electrode materials will  
36  
37 offer additional opportunities for future developments of energy storage devices.  
38  
39  
40  
41  
42  
43

44  
45 We exploit, in this work, the capacitive properties of NiMnCr LDHs for energy storage and  
46  
47 their improvement through hybridization with carbon spheres (CS) supported on nickel foam  
48  
49 (NF) collector. The NiMnCr LDH coated on carbon spheres and supported on Ni foam  
50  
51 (NiMnCr LDHs@CS/NF) was fabricated through a hydrothermal process. The hierarchical  
52  
53 structure of the NiMnCr LDHs@CS/NF composite exhibited improved capacity of  $569 \text{ C g}^{-1}$   
54  
55 at  $3 \text{ A g}^{-1}$  with good reversibility and stability. The NiMnCr LDHs@CS/NF electrode retained  
56  
57  
58  
59  
60  
61  
62  
63  
64  
65

1 ~83% and 76% of its initial value after 5,000 and 10,000 cycles, respectively, better than that  
2  
3 achieved by NiMnCr LDHs/NF composite (65% and 54%) under otherwise identical  
4  
5 experimental conditions. Furthermore, a hybrid supercapacitor was fabricated using NiMnCr  
6  
7 LDHs@CS/NF and FeOOH/NF respectively as the positive and negative electrodes. The  
8  
9 NiMnCr LDHs@CS/NF// FeOOH/NF device reached an energy density of 48 Wh kg<sup>-1</sup> at a  
10  
11 power density of 402.7 W kg<sup>-1</sup>. A home-designed windmill device was successfully driven by  
12  
13 one as-fabricated supercapacitor device. Additionally, two as-fabricated hybrid supercapacitor  
14  
15 cells in series were used to light up a yellow LED and a red LED in parallel for ~111 s and  
16  
17 ~343 s, respectively.  
18  
19  
20  
21  
22  
23  
24  
25  
26  
27

## 28 **2. Experimental section**

### 29 **2.1. Preparation of carbon spheres on nickel foam (CS/NF)**

30  
31 Carbon spheres coated on Ni foam (CS/NF) nanocomposite was obtained through a simple  
32  
33 one-step hydrothermal process [25], see **Supporting Information** for more details.  
34  
35  
36  
37  
38

### 39 **2.2. Synthesis of NiMnCr LDHs@CS/NF**

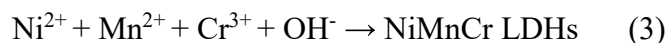
40  
41 Typically, Mn(NO<sub>3</sub>)<sub>2</sub>·4H<sub>2</sub>O (0.45 mmol), Cr(NO<sub>3</sub>)<sub>3</sub>·9H<sub>2</sub>O (0.075 mmol), CO(NH<sub>2</sub>)<sub>2</sub> (3.5 mmol)  
42  
43 and NH<sub>4</sub>F (8 mmol) were placed in MQ water (30 mL) under stirring until formation of a  
44  
45 homogeneous solution. The CS/NF was introduced into the solution, and the mixture was  
46  
47 placed in an autoclave. The mixture was heated at 120 °C. After 12 h, the autoclave was cooled  
48  
49 to RT, and NiMnCr LDHs@CS/NF was rinsed copiously with MQ water and ethanol, and dried  
50  
51 for 24 h at 60 °C. It is noteworthy to mention that the nickel foam acts as a support, but also as  
52  
53 a Ni source for LDHs formation during the hydrothermal reaction.  
54  
55  
56  
57  
58  
59  
60  
61  
62  
63  
64  
65

### 2.3. Synthesis of FeOOH nanorods

In a typical synthesis,  $\text{Fe}(\text{NO}_3)_3 \cdot 9\text{H}_2\text{O}$  (1 mmol),  $\text{CO}(\text{NH}_2)_2$  (5 mmol) and  $\text{NH}_4\text{F}$  (1 mmol) were placed deionized water (30 mL) under stirring till formation of a homogeneous solution. The resulting aqueous solution was placed in an autoclave and heated at  $120\text{ }^\circ\text{C}$  for 6 h. After being cooled naturally to RT, the sample was copiously rinsed with deionized water and ethanol under ultrasonication, and dried for 24 h at  $60\text{ }^\circ\text{C}$ . Then, the precursors were converted to FeOOH through annealing for 2 h at  $350\text{ }^\circ\text{C}$ .

### 3. Results and discussion

The preparation of NiMnCr LDHs@CS/NF electrode is illustrated in **Figure 1a**. Carbon spheres (CS) were first decorated on NF by a simple hydrothermal decomposition of glucose at  $190\text{ }^\circ\text{C}$  for 4 h, followed by coating of NiMnCr LDHs at  $120\text{ }^\circ\text{C}$  for 12 h using  $\text{Cr}(\text{NO}_3)_3 \cdot 9\text{H}_2\text{O}$ ,  $\text{Mn}(\text{NO}_3)_2 \cdot 4\text{H}_2\text{O}$ ,  $\text{CO}(\text{NH}_2)_2$  and  $\text{NH}_4\text{F}$  precursors. The chemical process can be described using equations (1-3) below:



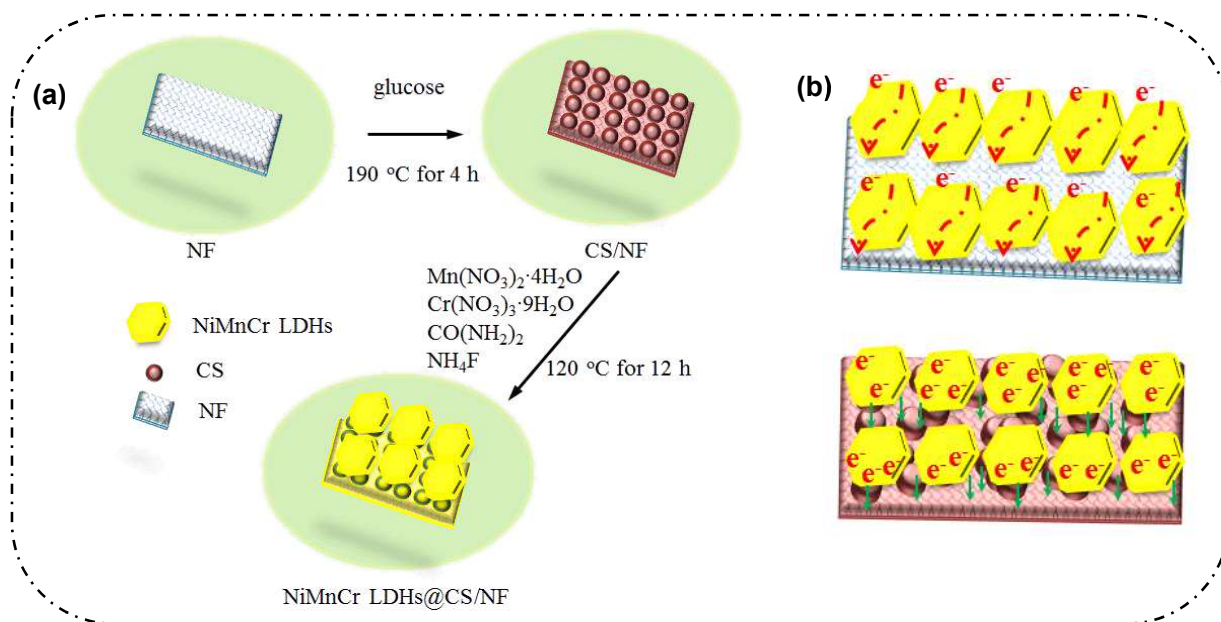


**Figure 1:** Illustrations of (a) the preparation of NiMnCr LDHs@CS/NF electrode using a two step hydrothermal process, (b) charge transport process in NiMnCr LDHs/NF and NiMnCr LDHs@CS/NF electrodes.

The reactions, under the hydrothermal conditions, mainly involve progressive hydrolysis of  $\text{NH}_4\text{F}$  and decomposition of  $\text{CO}(\text{NH}_2)_2$ , forming the NiMnCr LDHs on the NF substrate. It is noteworthy to mention that  $\text{Ni}^{2+}$  required for NiMnCr LDH formation originates from the Ni foam dissolution under our experimental conditions. Indeed, during the hydrothermal process,  $\text{NH}_4\text{F}$  dissolves nickel oxides on the Ni foam to release  $\text{Ni}^{2+}$  in the solution. As illustrated in **Figure 1b**, the existence of CSs layer on the NF surface could act as the bridge between NiMnCr LDHs and NF, which could decrease the length of charge transfer and facilitate the charge transfer, further promoting the electrochemical kinetics. For comparison, a control sample consisting of NiMnCr LDHs/NF was prepared in the same manner, but in the absence of CS.

**Fig. 2a** displays the XRD patterns of as-obtained materials. The patterns comprise several

typical diffraction peaks of LDHs at 11.4°, 24.1°, 31.4°, 33.4°, 38.7°, 41.2°, 59.9° and 63.6° ascribed respectively to the (006), (009), (012), (015), (018), (110), and (113) planes. At the same time, as a negative electrode candidate for hybrid supercapacitors, the XRD pattern of FeOOH nanorods was also recorded (**Fig. S1**) and shows diffraction peaks at 28.4°, 33.4°, 35.9°, 39.5°, 41.2°, 46.6°, 48.9°, 56.3°, 62.6°, and 64.1°, which are indexed to the (130), (400), (211), (301), (031), (411), (141), (060), (002) and (112) diffraction planes (JCPDS card no. 18-0639), respectively. Notably, FeOOH nanorods were not completely pure with some weak peaks observed at 30.4°, 35.7°, 43.5°, and 57.5°, corresponding to the (220), (311), (400), and (511) diffraction planes of Fe<sub>3</sub>O<sub>4</sub> (JCPDS card no. 75-0449) [26].

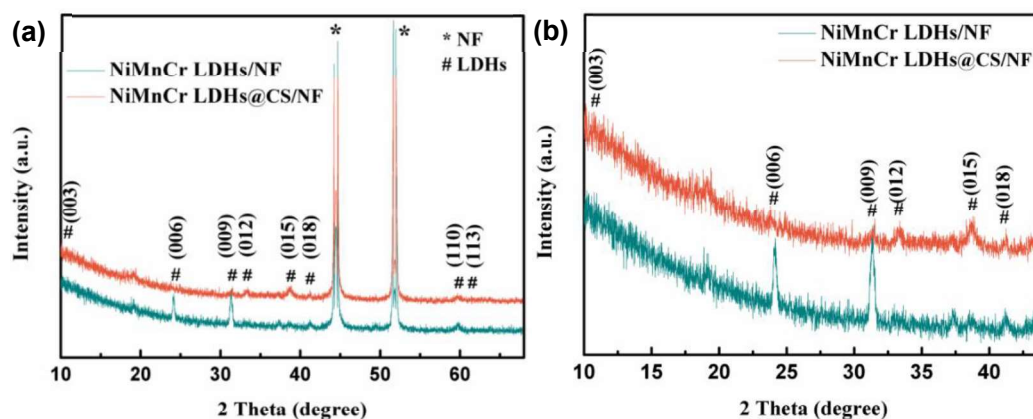


**Figure 2:** (a) XRD patterns of NiMnCr LDHs/NF and NiMnCr LDHs@CS/NF, (b) magnified patterns in the 10–44° range.

FTIR spectra of CS/NF, NiMnCr LDHs/NF and NiMnCr LDHs@CS/NF were recorded in **Fig. S2**. The peak at  $\sim 3387\text{ cm}^{-1}$  is attributed to the stretching of hydroxyl groups of water molecules, and the bands at  $\sim 1342$  and  $826\text{ cm}^{-1}$  prove the presence of  $\text{CO}_3^{2-}$ . Furthermore, the peaks in NiMnCr LDHs/NF and NiMnCr LDHs@CS/NF FTIR spectra  $< 800\text{ cm}^{-1}$  correspond to the stretching and bending vibration modes of M-O, proving the successful synthesis of the

LDHs on CS/NF [20].

The morphology of CS/NF, NiMnCr LDHs/NF and NiMnCr LDHs@CS/NF was assessed by scanning electron microscopy (SEM). **Fig. 3a** and **b** depicts the low and high magnifications images of the carbon spheres used herein to improving the electrical conductivity of the material and the contact area. A dense layer of CS of ~400 nm in diameter was formed on the NF surface.

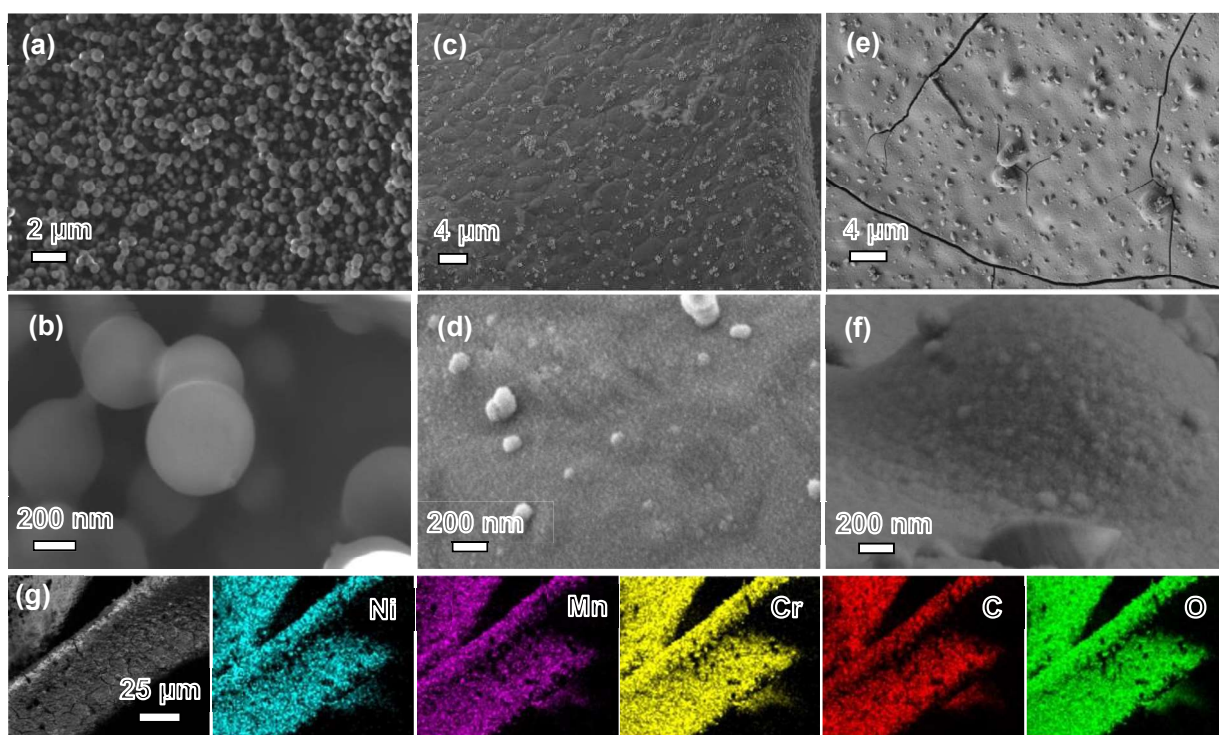


**Figure 3:** SEM images of (a, b) CS/NF, (c, d) NiMnCr LDHs/NF and (e, f) NiMnCr LDHs@CS/NF. (g) EDS elemental mapping images of Ni, Mn, Cr, C and O of NiMnCr LDHs@CS/NF.

All the spheres exhibit a smooth surface, suggesting the homogeneous polymerization of glucose after the hydrothermal process (**Fig. 3b**). **Figure 3c,d** displays a NF directly coated with NiMnCr LDHs in absence of CS support. A flat lunar surface was clearly visible, which contrasts with NiMnCr LDHs supported on CS/NF where an uneven shape with rounded small

1 protrusions (**Figure 3e, f**) was observed. Due to the thick NiMnCr LDHs layer ( $\sim 1 \mu\text{m}$ ), the  
2  
3 CSs were not any longer visible in the SEM image even from the cross-sectional image of  
4  
5 NiMnCr LDHs@CS/NF in **Fig. S3**, suggesting that the CSs were completely coated by  
6  
7 NiMnCr LDHs. This could be also the reason why no obvious CS diffraction peaks in the XRD  
8  
9 pattern of NiMnCr LDHs@CS/NF were observed in **Figure 2**. This morphology is expected to  
10  
11 enhance the material/electrolyte contact area, which would improve the overall electrode  
12  
13 performance. As illustrated in **Figure 3g** and **Figure S3b**, the EDS elemental mapping of  
14  
15 NiMnCr LDHs@CS/NF revealed Mn, Ni, Cr, C, and O elements distributed homogeneously  
16  
17  
18  
19  
20  
21  
22  
23 on the material.

24  
25  
26  
27  
28  
29  
30  
31  
32  
33  
34  
35  
36  
37  
38  
39  
40  
41  
42  
43  
44  
45  
46  
47  
48  
49  
50  
51  
52  
53  
54  
55  
56  
57  
58  
59  
60  
61  
62  
63  
64  
65  
Furthermore, transmission electron microscopy (TEM) was performed to assess the  
morphology and structure of NiMnCr LDHs@CS/NF (**Figure 4**). **Figure 4b,c** depicts the high  
high-resolution TEM (HRTEM) images of NiMnCr LDHs@CS/NF, revealing two types of  
lattice spacings of 0.26 and 0.38 nm, ascribed respectively to (012) and (006) planes of LDHs.  
These findings are in accordance with the XRD analysis in **Figure 2**. **Figure 4d** exhibits the  
corresponding EDS elemental mapping where Ni, Mn, Cr, C and O elements are  
homogeneously distributed, matching the results presented in **Figure 3g** and **Figure S3b**.

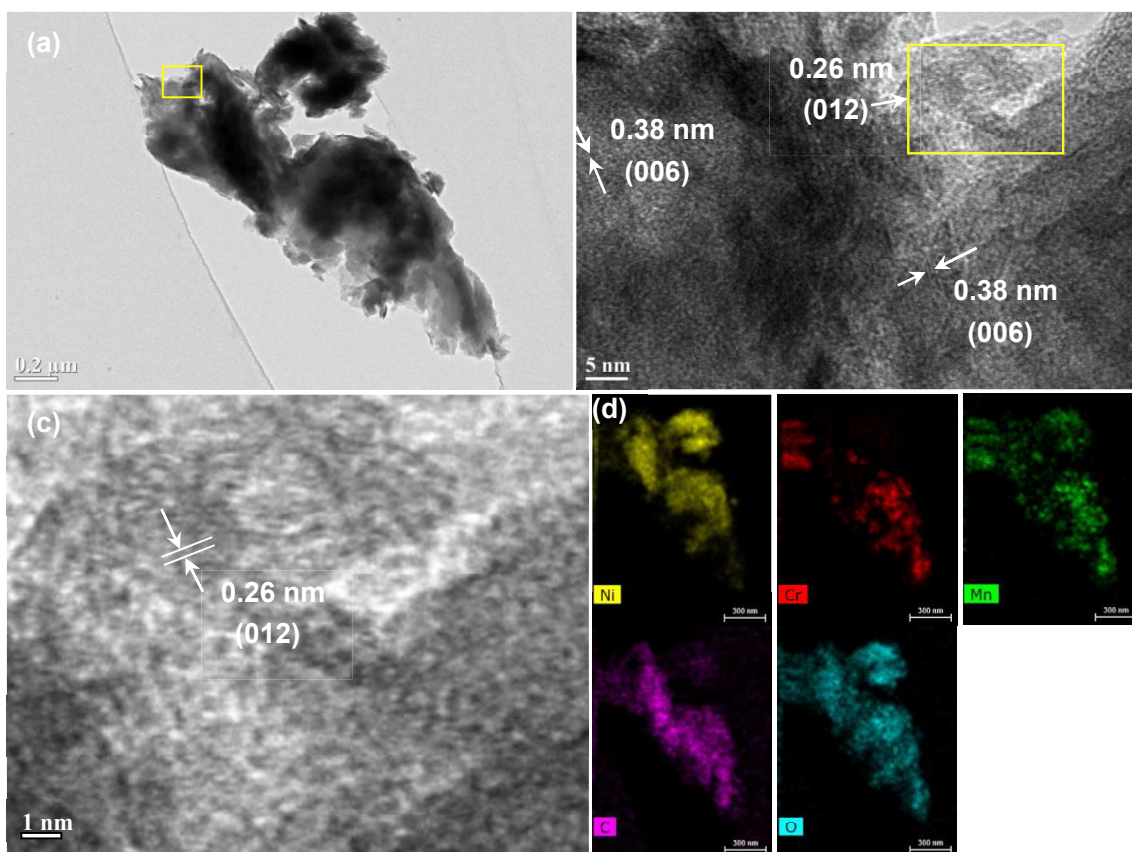


**Figure 4:** (a) TEM and (b) high-resolution TEM images of NiMnCr LDHs@CS/NF, (d) is the corresponding EDS elemental mapping of Mn, Ni, Cr, C, and O elements.

X-ray photoelectron spectroscopy (XPS) was acquired to evaluate the elemental composition of NiMnCr LDHs/NF (**Fig. S4**) and NiMnCr LDHs@CS/NF (**Figure 5a**) composites. The wide scan XPS spectrum revealed that the electrode material consists of Ni<sub>2p</sub>, Mn<sub>2p</sub>, Cr<sub>2p</sub>, C<sub>1s</sub>, and O<sub>1s</sub> elements, in agreement with the elemental composition of the material.

The Ni<sub>2p</sub> high-resolution spectrum of NiMnCr LDHs@CS/NF composite (**Figure 5b**) comprises two peaks due to Ni<sub>2p3/2</sub> and Ni<sub>2p1/2</sub> located respectively at 854.8 and 872.5 eV, and satellite peaks [27]. The presence of the satellite peaks is a good indication that the nickel in the LDH is in its +2 oxidation state.

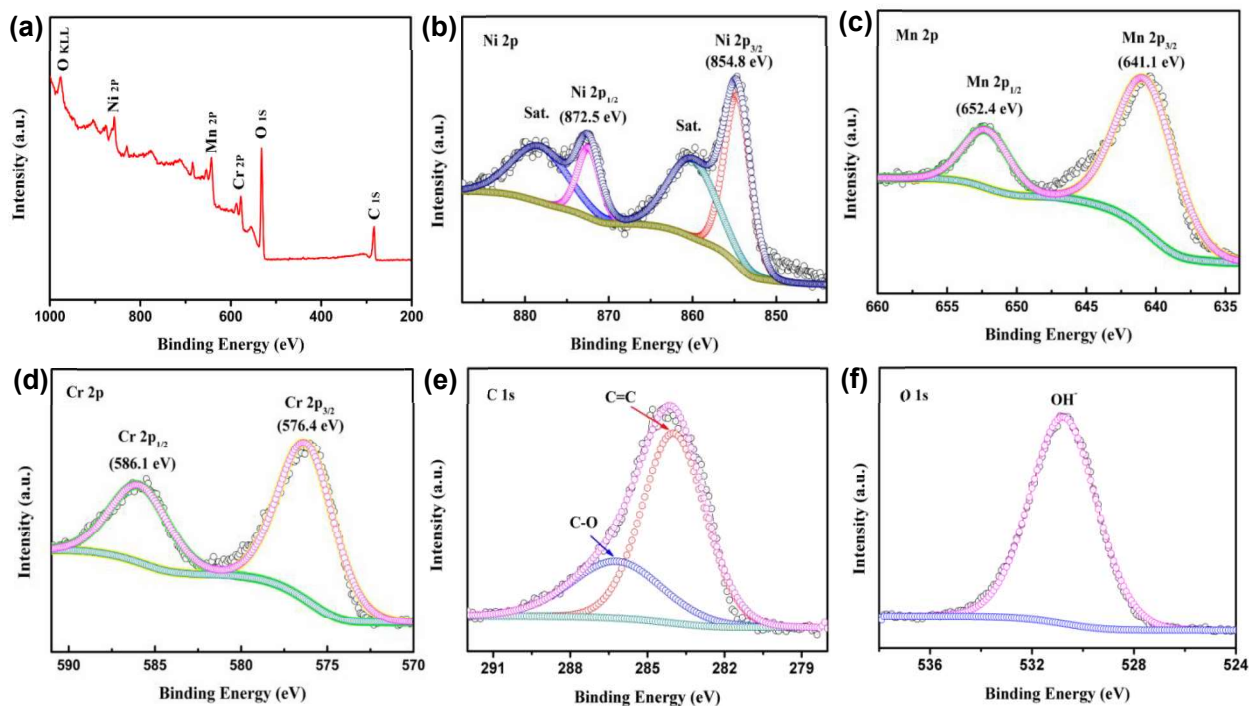


**Figure 5:** XPS analysis of NiMnCr LDHs@CS/NF: (a) Full scan, and core level plots of (b) Ni<sub>2p</sub>, (c) Mn<sub>2p</sub>, (d) Cr<sub>2p</sub>, (e) C<sub>1s</sub> and (f) O<sub>1s</sub>.

**Figure 5c** depicts the Mn<sub>2p</sub> core level spectrum of NiMnCr LDHs@CS/NF composite, which can be deconvoluted into two peaks at 652.4 and 641.1 eV assigned respectively to Mn<sub>2p1/2</sub> and Mn<sub>2p3/2</sub> peaks, indicating the presence of Mn<sup>3+</sup> [28, 29]. It is highly convenient to oxidize Mn<sup>2+</sup> to Mn<sup>3+</sup> due to the low redox potential ( $E^0[\text{Mn}(\text{OH})_3/\text{Mn}(\text{OH})_2]=0.1$  V) under alkaline conditions. The Cr<sub>2p</sub> core level spectrum of NiMnCr LDHs@CS/NF composite can be deconvoluted in two bands at 586.1 and 576.4 eV ascribed respectively to Cr<sub>2p1/2</sub> and Cr<sub>2p3/2</sub>, suggesting that Cr is trivalent [30] (**Figure 5d**). **Figure 5e** displays the C<sub>1s</sub> core level spectrum, which can be curve-fitted with two components at 284.1 eV (C=C) and 286.4 eV (C-O). The O<sub>1s</sub> core level spectrum can be curve-fitted with a single component derived from –OH groups in LDHs (**Figure 5f**). Similarly, XPS analysis of NiMnCr LDHs/NF composite revealed a comparable composition to that of NiMnCr LDHs@CS/NF composite with a slight shift of the

1 binding energies of Ni<sub>2p</sub>, Mn<sub>2p</sub> and Cr<sub>2p</sub> (**Figure S4**).

2  
3 The real electrochemical effective surface area (*A*) of the electrodes was determined by  
4 chronocoulometry using 0.1 mM K<sub>3</sub>[Fe(CN)<sub>6</sub>] in 0.1 M KCl as a redox active probe, and the  
5 charge produced by the redox reaction at the electrodes based on the Anson equation (4):  
6  
7  
8  
9

$$10 \quad Q(t) = \frac{2nFAC_0D_0^{\frac{1}{2}}t^{\frac{1}{2}}}{\pi^{\frac{1}{2}}} + Q_{dl} + Q_{ads} \quad (4)$$

11  
12  
13  
14  
15  
16  
17 Where *c* is the substrate concentration, *n* is the number of electrons transferred, *F* corresponds  
18 to the Faraday constant (9.6485×10<sup>5</sup> C mol<sup>-1</sup>), *A* (cm<sup>2</sup>) represents the surface area of the  
19 working electrode, *C*<sub>0</sub> (mol cm<sup>-3</sup>) is the initial concentration of the redox mediator, *D* is the  
20 diffusion coefficient (7.6×10<sup>-6</sup> cm<sup>2</sup> s<sup>-1</sup>), *Q*<sub>dl</sub> is the double layer charge, *Q*<sub>ads</sub> is the Faradaic  
21 charge, charge.  
22  
23  
24  
25  
26  
27  
28  
29

30 By plotting the charge vs *t*<sup>1/2</sup>, the electrode surface area can be determined from the slope  
31 (**Figure S5**). Using equation 4, active surface areas of 426 and 590 cm<sup>2</sup> were calculated for  
32 NiMnCr LDHs/NF and NiMnCr LDHs@CS/NF, respectively, highlighting the favorable  
33 electrochemical properties of the NiMnCr LDHs@CS/NF electrode for energy storage.  
34  
35  
36  
37  
38  
39  
40  
41

42 **Figure 6a** presents the CV curves of NF, CS/NF, NiMnCr LDHs/NF and NiMnCr  
43 LDHs@CS/NF (scan rate=100 mV s<sup>-1</sup>). All the curves have a similar shape; all of them exhibit  
44 obvious redox peaks, which could be attributed to Ni<sup>2+</sup>/Ni<sup>3+</sup> in the NiMnCr LDHs. Notably, the  
45 redox peaks in the CV of CS/NF originate most likely from nickel oxide present on the NF  
46 surface. Furthermore, NiCr LDHs/NF and NiMn LDHs/NF were also synthesized and their  
47 performance was assessed under the same conditions as well (**Figure S6a**), and obviously  
48 MnCr LDHs/NF and NiCr LDHs/NF showed relatively smaller CV areas. Without the Ni  
49  
50  
51  
52  
53  
54  
55  
56  
57  
58  
59  
60  
61  
62  
63  
64  
65

1 participation, MnCr LDHs was coated on carbon paper (MnCr LDHs/CP), and there are no  
2  
3 apparent redox peaks in the CV plots (**Figure S6b**). In contrast, the CV curves of NiCr  
4  
5 LDHs/NF, NiMn LDHs/NF and NiMnCr LDHs/NF presented apparent similar redox peaks,  
6  
7 further proving that the redox features are due to Ni<sup>2+</sup>/Ni<sup>3+</sup> in the NiMnCr LDHs. Compared  
8  
9 with NiCr LDHs/NF and NiMn LDHs/NF, NiMnCr LDHs/NF exhibited the highest current  
10  
11 response along with a slight shift, which could be a consequence of a synergistic effect of Ni,  
12  
13 Mn and Cr elements. From **Figure 6b**, we can see a slight shift of the redox peak potential as  
14  
15 the scan rate increases; this is a good indication of a good conductivity and facile ion transport  
16  
17 kinetics. Furthermore, to separate the diffusion controlled capacity and capacitive capacity, the  
18  
19 kinetic analysis was performed (**Figure S7**). Usually, the plot of log(*i*) of anodic and cathodic  
20  
21 peak currents vs. log(*v*) allows to determine the contribution of the capacitive process:  $i = av^b$ ,  
22  
23 *i* and *v* are respectively the current and scan rate. When the variable  $b=1$ , the capacitive process  
24  
25 controls the electrochemical reaction, and when the variable  $b=0.5$ , the electrochemical  
26  
27 reaction is derived from a semi-infinite diffusion process (Faradaic mode). As depicted in  
28  
29 **Figure S7a**, *b* values of 0.52 and 0.56 were calculated for NiMnCr LDHs@CS/NF from the  
30  
31 anode and cathode peak currents, respectively at scan rates of 10, 20, 50, 75 and 100 mV s<sup>-1</sup>.  
32  
33 These values are comprised between 0.5 and 1, signifying that both capacitive and battery-type  
34  
35 processes contribute to the charge storage mechanism. The whole process can be described  $i =$   
36  
37  $k_1v + k_2v^{1/2}$ , where  $k_1$  and  $k_2$  can be deduced respectively from the slope and the y-axis intercept  
38  
39 of the  $1/v^{1/2}$  vs.  $v^{1/2}$  plot. We can see from **Figure S7b** that the capacitive contribution ratio at  
40  
41 10 mV s<sup>-1</sup> is about 20.1%, and increases to 44.3% at 100 mV s<sup>-1</sup>.  
42  
43  
44  
45  
46  
47  
48  
49  
50  
51  
52  
53  
54  
55  
56  
57

58 **Figure 6c** indicates that in the presence of CS, NiMnCr LDHs@CS/NF composite  
59  
60

possesses larger charging/discharging time, suggesting higher specific capacity. In fact, a specific capacity of 569 C g<sup>-1</sup> was determined at 3 A g<sup>-1</sup>, surpassing that of NF (24.4 C g<sup>-1</sup>), CS/NF (88 C g<sup>-1</sup>) and NiMnCr LDHs/NF (173.2 C g<sup>-1</sup>). To establish the performance of NiMnCr LDHs@CS/NF composite, galvanostatic charge-discharge (GCD) plots were measured at various current densities (Figure 6d).

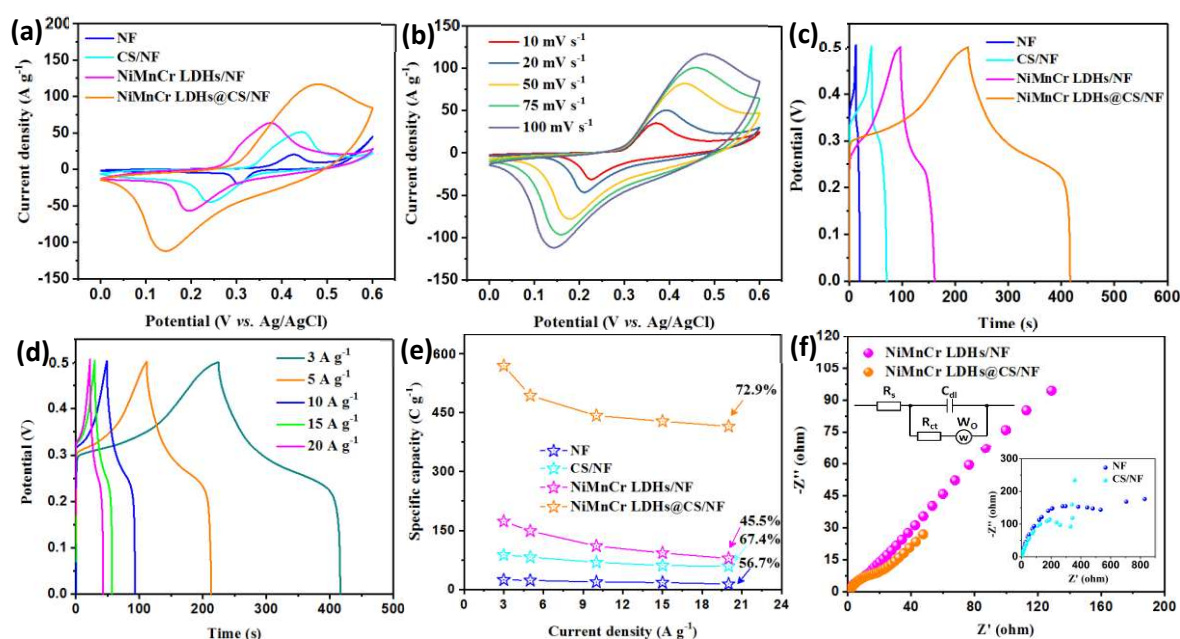


**Figure 6:** The electrochemical behavior of the electrodes in KOH (2 M) solution. (a) CV curves acquired at 100 mV s<sup>-1</sup>, (b) CV plots of NiMnCr LDHs@CS/NF recorded at different scan rates, (c) GCD plots of the electrodes at 3 A g<sup>-1</sup>, (d) GCD plots of the electrodes at various current densities, (e) Specific capacity of the electrodes at different current densities, (f) Electrochemical impedance plots of NiMnCr LDHs /NF and NiMnCr LDHs@CS/NF acquired at open circuit potential (frequency range = 0.01 Hz to 100 kHz), the inset in the top-right of (f) is the corresponding equivalent circuit and the inset in the bottom of (f) are electrochemical impedance spectra of NF and CS/NF recorded at open circuit potential (frequency range = 0.01 Hz to 100 kHz).

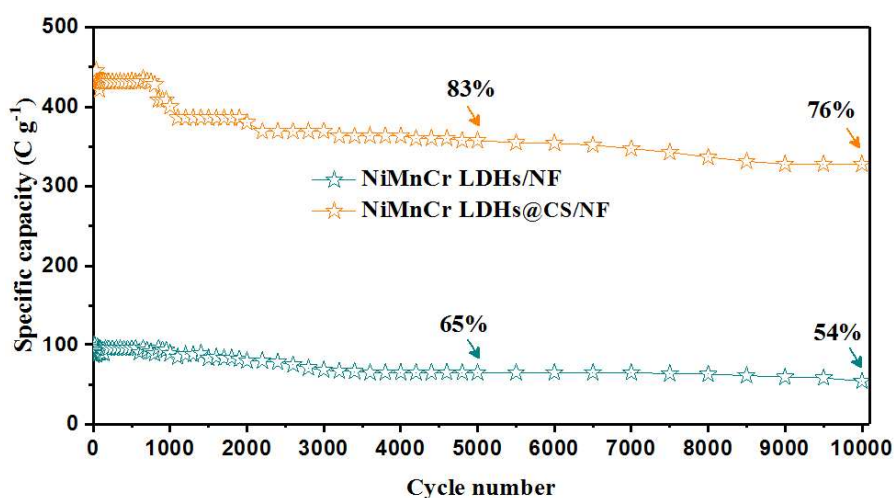
Furthermore, Figure 6e and Table S2 summarize the capacity values of the various

1 electrodes at different current densities, which are determined using equation S2  
2  
3 **(Supplementary Information)** from the values in **Figure 6d**. The results clearly revealed that  
4  
5 NiMnCr LDHs/NF and NiMnCr LDHs@CS/NF exhibit higher specific capacity values than  
6  
7 NF and CS/NF with NiMnCr LDHs@CS/NF featuring a better rate performance and specific  
8  
9 capacity of 569, 493.2, 442.2, 427.9 and 414.7 C g<sup>-1</sup> at respectively 3, 5, 10, 15 and 20 A g<sup>-1</sup>.  
10  
11 The specific capacity value remained high (73% of the specific capacity recorded at 3 A g<sup>-1</sup>)  
12  
13 even at 20 A g<sup>-1</sup>. At the same time, the IR drop of NiMnCr LDHs@CS/NF composite was  
14  
15 lower (8 mV) than that of NiMnCr LDHs/NF (12 mV), indicating a relatively lower charge-  
16  
17 transfer resistance; this property contributes for the better rate performance of NiMnCr  
18  
19 LDHs@CS/NF. The equivalent circuit for impedance analysis is illustrated in the inset of  
20  
21 **Figure 6f** ( $R_{ct}$ ,  $R_s$ ,  $C_{dl}$ , and  $W_o$  stand respectively for the charge-transfer resistance, internal  
22  
23 resistance, double-layer capacitance, and Warburg element). From these measurements (**Figure**  
24  
25 **6f**), we can see that compared to pure NF (622.7 Ohm cm<sup>-2</sup>), CS/NF exhibits a smaller charge-  
26  
27 transfer resistance (379.6 Ohm cm<sup>-2</sup>). Even though NiMnCr LDHs@CS/NF composite  
28  
29 possesses a relatively higher internal resistance (1.167 Ohm cm<sup>-2</sup>), it displays a smallest  
30  
31 semicircle in the high frequency region related to the electrochemical reaction process, which  
32  
33 means a lowest charge-transfer resistance of 15.03 Ohm cm<sup>-2</sup>, smaller than that NiMnCr  
34  
35 LDHs/NF (18.28 Ohm cm<sup>-2</sup>) (**Table S3**), consistent with the low IR drop. The results indicate  
36  
37 that the existence of CS could facilitate the charge transfer and promote the electrochemical  
38  
39 kinetics, as illustrated in **Figure 1b**.  
40  
41  
42  
43  
44  
45  
46  
47  
48  
49  
50  
51  
52  
53  
54  
55

56 As observed in **Figure 7**, NiMnCr LDHs@CS/NF electrode displays good stability after  
57  
58 10,000 cycles at 20 A g<sup>-1</sup>. The electrode retained ~76% of its initial value, which is better than  
59  
60  
61  
62  
63  
64  
65

1 ~54% achieved by NiMnCr LDHs/NF under the same cycling conditions.

2  
3 **Figure S8** depicts the SEM and EDS elemental mapping images of NiMnCr LDHs/NF and  
4 NiMnCr LDHs@CS/NF after cycling. After 10000 cycles, most of the NiMnCr LDHs on NF  
5  
6 disappear in NiMnCr LDHs/NF composites (**Figure S8a**), but there are still Ni, Mn, Cr, C, and  
7  
8 O elements distributed homogeneously on the material, with the existence of K element from  
9  
10 the KOH electrolyte. For the NiMnCr LDHs@CS/NF composite, cracks appeared in the SEM  
11  
12 image of the electrode material and the CS features become evident. Similarly, EDX mapping  
13  
14 showed the existence of Ni, Mn, Cr, C, O, and K species (**Figure S8b**). NiMnCr LDHs@CS/NF  
15  
16 composite exhibited a more stable morphology compared to NiMnCr LDHs/NF owing to the  
17  
18 presence of CSs.



44 **Figure 7:** Cycling performance of NiMnCr LDHs@CS/NF and NiMnCr LDHs/NF at a  
45 constant current density of 20 A g<sup>-1</sup>.

46  
47  
48  
49  
50  
51 XPS analysis of the NiMnCr LDHs/NF and NiMnCr LDHs@CS/NF electrode materials  
52  
53 after cycling was further acquired (**Figures S9 and S10**). From the XPS survey spectra in  
54  
55 **Figure S9a and S10a**, we can see that both NiMnCr LDHs/NF and NiMnCr LDHs@CS/NF  
56  
57 still comprise Ni<sub>2p</sub>, Mn<sub>2p</sub>, C<sub>1s</sub> and O<sub>1s</sub> elements, while Cr<sub>2p</sub> was absent. An additional peak due  
58  
59  
60  
61

1 to  $K_{2p}$ , originating from the KOH electrolyte, appeared. Furthermore, by analyzing the elements  
2  
3 composition changes (**Table S1**), one clearly sees that NiMnCr LDHs/NF experienced a  
4  
5 significant loss as compared to NiMnCr LDHs@CS/NF, which is in accordance with the  
6  
7 cycling performance data in **Figure 7**. The existence of CS could help release the deformation  
8  
9 and stress during the charging/discharging cycles to immobilize the NiMnCr LDHs layer,  
10  
11 further improving the mechanical stability [31].  
12  
13  
14  
15

16  
17 Finally, a hybrid supercapacitor was assembled using NiMnCr LDHs@CS/NF (positive  
18  
19 electrode) and FeOOH/NF (negative electrode). The morphology of FeOOH consists of  
20  
21 nanorods (see SEM image in **Figure S11**). The electrochemical behavior of the FeOOH/NF  
22  
23 electrode was examined in KOH (2 M) aqueous. **Figure S12a** depicts the CV curves (-1 V to  
24  
25 -0.5 V) of FeOOH/NF electrode at various scan rates, which implies its potential use as a  
26  
27 negative electrode. Using equation S2 (**Supplementary Information**), the specific capacity of  
28  
29 FeOOH/NF was calculated to be 126, 88.8, 72.8, 59.9, 51.6 and 49.1 C g<sup>-1</sup> respectively at 1, 2,  
30  
31 3, 5, 10 and 15 A g<sup>-1</sup>, as illustrated in **Figure S12b** and **c**, which proves that FeOOH could be  
32  
33 a promising negative material.  
34  
35  
36  
37  
38  
39  
40  
41

42 The NiMnCr LDHs@CS/NF//FeOOH/NF hybrid supercapacitor possesses a great  
43  
44 potential window, which could be extended to 1.8 V (**Figure 8a**). Interestingly, the CV curves  
45  
46 display a similar shape, suggesting an excellent capacitive performance. Obviously, there exists  
47  
48 a polarization phenomenon above 1.7 V, so the potential window was chosen as 0-1.7 V to  
49  
50 reduce the damage to the electrode. **Figure S13** depicts the CV plots of the hybrid  
51  
52 supercapacitor in the potential window between 0 and +1.7 V acquired at various scan rates.  
53  
54  
55  
56  
57  
58 Upon increasing the scan rate, one sees a shift of the redox peak potential; this may be attributed  
59  
60  
61  
62  
63  
64  
65

to internal resistance increase at higher scan rates.

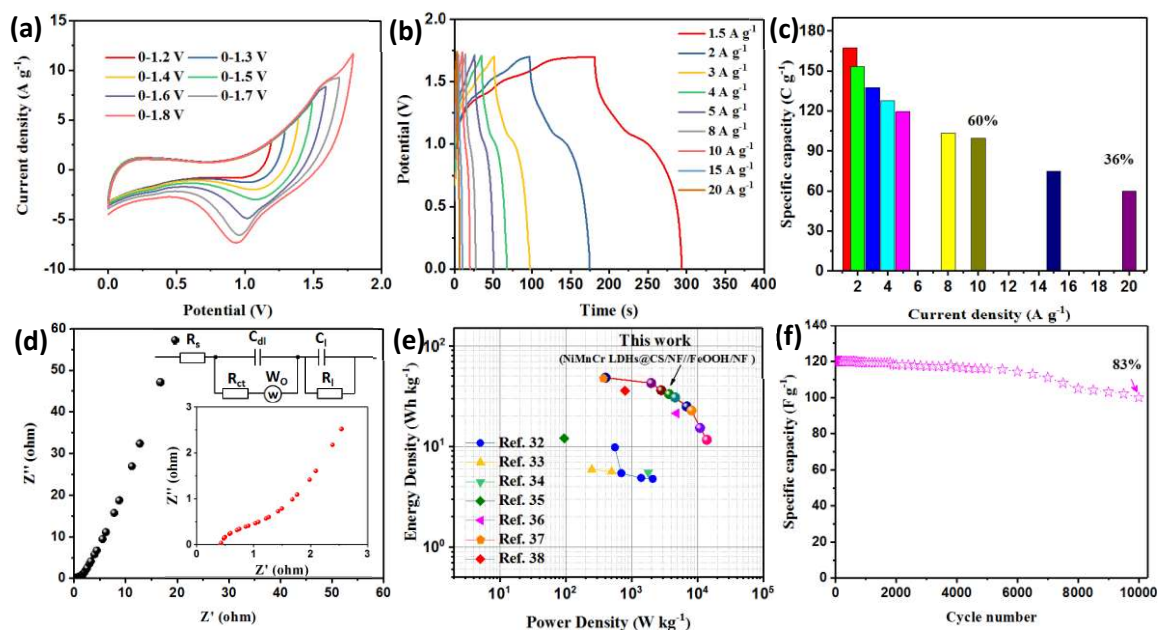


**Figure 8:** Electrochemical characterization of the NiMnCr LDHs@CS/NF//FeOOH/NF hybrid supercapacitor. (a) CV plots acquired in different potential windows at 100 mV s<sup>-1</sup>, (b) GCD plots acquired at various current densities, (c) Specific capacity at various current densities, (d) EIS curves recorded in the 0.01 Hz and 100 kHz frequency range. The inset up-right in (d) is the corresponding equivalent circuit. (e) Ragone plots, (f) Cycling performance of NiMnCr LDHs@CS/NF//FeOOH hybrid supercapacitor at 5 A g<sup>-1</sup>.

**Figure 8b** displays the GCD curves of the NiMnCr LDHs@CS/NF//FeOOH device at various current densities, demonstrating high coulombic efficiency (**Table S4**). The specific capacity values, deduced from the discharging curves in **Figure 8b**, are displayed in **Figure 8c**. The NiMnCr LDHs@CS/NF//FeOOH/NF hybrid supercapacitor achieved specific capacity values of 167.4, 153.4, 137.5, 129.6, 103.6, 99.6, 74.7 and 59.8 C g<sup>-1</sup> respectively at 1.5, 2, 3, 4, 5, 8, 10, 15 and 20 A g<sup>-1</sup>, which shows a good rate performance (60% of areal capacity was maintained at 10 A g<sup>-1</sup> and 36% of areal capacity was retained even at 20 A g<sup>-1</sup>).

Additionally, the hybrid supercapacitor was characterized by EIS in the 0.01 Hz and 100

1 kHz frequency range; the equivalent circuit for impedance analysis was illustrated in the inset  
2  
3 of **Figure 8d** ( $R_{ct}$ ,  $R_s$ ,  $C_{dl}$ ,  $W_o$ ,  $C_l$  and  $R_l$  are respectively the charge-transfer resistance, internal  
4  
5 resistance, double-layer capacitance, Warburg element, limit capacitance and limit resistance).  
6  
7 From the Nyquist plot, one clearly sees a semicircle (high-frequency range) associated with the  
8  
9 charge transfer resistance, and a straight line in the low-frequency region. The  $R_s$  and  $R_{ct}$  values  
10  
11 are determined to be about  $\sim 0.45$  and  $\sim 0.49$  ohm  $\text{cm}^{-2}$ , respectively.  
12  
13  
14  
15  
16

17 To achieve a full electrochemical characterization of the as-prepared hybrid  
18  
19 supercapacitor, the Ragone plot is provided in **Figure 8e**. The NiMnCr  
20  
21 LDHs@CS/NF//FeOOH/NF device attained a great energy density of  $48 \text{ Wh kg}^{-1}$  at a power  
22  
23 density of  $402.7 \text{ W kg}^{-1}$ , which is larger than that of NiFe LDH/rGO/NF// MC/NF ( $9.8 \text{ Wh kg}^{-1}$   
24  
25 at  $560 \text{ W kg}^{-1}$ ) [32], CoMn-LDH/AC ( $5.9 \text{ Wh kg}^{-1}$  at  $250 \text{ W kg}^{-1}$ ) [33],  $\text{MnFe}_2\text{O}_4/\text{LiMn}_2\text{O}_4$   
26  
27 ( $5.5 \text{ Wh kg}^{-1}$  at  $1800 \text{ W kg}^{-1}$ ) [34], Ni-Co oxide/AC ( $12 \text{ Wh kg}^{-1}$  at  $95.2 \text{ W kg}^{-1}$ ) [35],  
28  
29  $\text{MnO}_2@\text{Co-Ni LDH}$  ( $21.3 \text{ Wh Kg}^{-1}$  at  $4.8 \text{ kW kg}^{-1}$ ) [36],  $\text{Co}_3\text{O}_4@\text{NiMn-LDH/Ni}$  ( $47.15 \text{ Wh}$   
30  
31  $\text{kg}^{-1}$  at  $376 \text{ W kg}^{-1}$ ) [37] and  $\text{CoS}_x/\text{Ni-Co LDH}$  nanocages ( $35.8 \text{ Wh kg}^{-1}$  at  $800 \text{ W kg}^{-1}$ ) [38]  
32  
33 hybrid supercapacitors. Even though the developed NiMnCr LDHs@CS/NF//FeOOH/NF  
34  
35 hybrid supercapacitor achieved good performance, there is room for improvement by applying  
36  
37 suitable negative materials. **Figure 8f** depicts the charging/discharging cycles at  $5 \text{ A g}^{-1}$ . The  
38  
39 hybrid supercapacitor maintained  $\sim 83\%$  of the original capacity after 10,000 cycles, signifying  
40  
41 a good stability of the energy storage device.  
42  
43  
44  
45  
46  
47  
48  
49  
50  
51  
52

53 To highlight the practical use of the as-fabricated supercapacitor device, it was applied for  
54  
55 operating a home-designed windmill device (**Fig. 9a** and **c**). The device comprises an engine  
56  
57 ( $1.5\text{-}9 \text{ V}$ ), windmill and one as-fabricated supercapacitor device. The windmill can be rotated  
58  
59  
60  
61  
62  
63  
64  
65

for about 25 s using the home-made device upon charging the supercapacitor at 1.7 V (**Fig. 9b** and **video 1**). Additionally, as is shown in **Fig. 9d**, two as-fabricated hybrid supercapacitor cells (SC) in series whose work potential window can reach 3.4 V (**Fig. 9b**) were used to supply electricity to red and yellow LEDs in parallel; the red LED was lighted for  $\sim 343$  s and the yellow one for  $\sim 111$  s at the same time (see **video 2**).

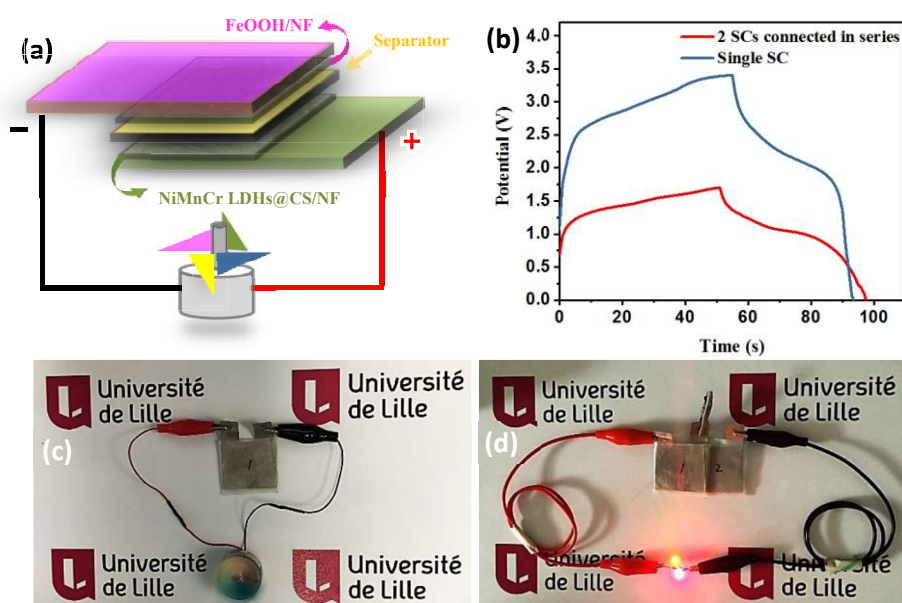


**Figure 9:** (a) Schematic diagram of the hybrid supercapacitor for windmill operation. (b) GCD plots of a single supercapacitor and two supercapacitors in series at  $3 \text{ A g}^{-1}$ . (c) Photograph of the home-designed windmill device. (d) Lightening of a red LED and a yellow LED in parallel by two supercapacitor cells in series.

#### 4. Conclusion

NiMnCr LDHs@CS/NF composites were prepared by a hydrothermal process, and successfully applied as efficient electrodes for supercapacitors. NiMnCr LDHs@CS/NF features a better rate performance and a specific capacity of  $569 \text{ C g}^{-1}$  at  $3 \text{ A g}^{-1}$ . Furthermore, NiMnCr LDHs@CS/NF electrode revealed good reversibility and stability. The electrode

1 retained ~76% of the specific capacity after 10,000 discharge cycles. Moreover, a hybrid  
2  
3 supercapacitor was assembled using NiMnCr LDHs@CS/NF as the positive electrode and  
4  
5 FeOOH/NF as the negative electrode. The device displayed an energy density of 48 Wh kg<sup>-1</sup> at  
6  
7 a power density of 402.7 W kg<sup>-1</sup> with good stability. A home-designed windmill device was  
8  
9 successfully driven for 25 s by the as-fabricated supercapacitor device and two as-fabricated  
10  
11 hybrid supercapacitor cells in series were used to light up a yellow LED and a red LED for  
12  
13 ~111 s and ~343 s, respectively. All of these findings demonstrate a promising practical energy  
14  
15 storage application of the as-fabricated hybrid supercapacitor devices.  
16  
17  
18  
19  
20  
21  
22  
23  
24

## 25 **Acknowledgements**

26  
27  
28 The authors thank the Centre National de la Recherche Scientifique (CNRS), the University  
29  
30 of Lille, and the Hauts-de-France region for financial support. Min Li thanks Chinese  
31  
32 government for the China Scholarship Council (CSC) fellowship. Mu. Naushad is grateful to  
33  
34 the Researchers Supporting Project number (RSP-2019/8), King Saud University, Riyadh,  
35  
36 Saudi Arabia for the support.  
37  
38  
39  
40  
41  
42  
43  
44

## 45 **References**

- 46  
47 [1] J. Yu, Q. Wang, D. O'Hare, L. Sun, Preparation of Two Dimensional Layered Double  
48  
49 Hydroxide Nanosheets and Their Applications, Chem. Soc. Rev. 46 (2017) 5950-5974.  
50  
51  
52 [2] X. Ma, X. Li, A.D. Jagadale, X. Hao, A. Abudula, G. Guan, Fabrication of Cu(OH)<sub>2</sub>@NiFe-  
53  
54 layered double hydroxide catalyst array for electrochemical water splitting, Int. J. Hydrogen  
55  
56 Energy 41 (2016) 14553-14561.  
57  
58  
59  
60  
61  
62  
63  
64  
65

- 1 [3] K. Fan, H. Chen, Y. Ji, H. Huang, P.M. Claesson, Q. Daniel, B. Philippe, H. Rensmo, F. Li,  
2  
3 Y. Luo, L. Sun, Nickel-vanadium monolayer double hydroxide for efficient electrochemical  
4  
5 water oxidation, *Nat. Commun.* 7 (2016) 11981.  
6  
7  
8 [4] Y. Zheng, J. Qiao, J. Yuan, J. Shen, A.-j. Wang, P. Gong, X. Weng, L. Niu, Three-  
9  
10 dimensional NiCu layered double hydroxide nanosheets array on carbon cloth for enhanced  
11  
12 oxygen evolution, *Electrochim. Acta* 282 (2018) 735-742.  
13  
14  
15 [5] J. Zhao, L. Cai, H. Li, X. Shi, X. Zheng, Stabilizing Silicon Photocathodes by Solution-  
16  
17 Deposited Ni-Fe Layered Double Hydroxide for Efficient Hydrogen Evolution in Alkaline  
18  
19 Media, *ACS Energy Lett.* 2 (2017) 1939-1946.  
20  
21  
22 [6] G. Zhang, L. Wu, A. Tang, X.-B. Chen, Y. Ma, Y. Long, P. Peng, X. Ding, H. Pan, F. Pan,  
23  
24 Growth Behavior of MgAl-Layered Double Hydroxide Films by Conversion of Anodic Films  
25  
26 on Magnesium Alloy AZ31 and Their Corrosion Protection, *Appl. Surf. Sci.* 456 (2018) 419-  
27  
28 429.  
29  
30  
31 [7] M. Wu, B. Chang, T. T. Lim, W. D. Oh, J. Lei, J. Mi, High-Sulfur Capacity and Regenerable  
32  
33 Zn-Based Sorbents Derived from Layered Double Hydroxide for Hot CoAl Gas  
34  
35 Desulfurization, *J. Hazard. Mater.* 360 (2018) 391-401.  
36  
37  
38 [8] G. Luo, K. S. Teh, Y. Xia, Z. Li, Y. Luo, L. Zhao, Z. Jiang, Construction of NiCo<sub>2</sub>O<sub>4</sub>@NiFe  
39  
40 LDHs Core/Shell Nanowires Array on Carbon Cloth for Flexible, High-Performance  
41  
42 Pseudocapacitor Electrodes, *J. Alloys Compds.* 767 (2018) 1126-1132.  
43  
44  
45 [9] S. Yu, Y. Zhang, G. Lou, Y. Wu, X. Zhu, H. Chen, Z. Shen, S. Fu, B. Bao, L. Wu, Synthesis  
46  
47 of NiMn-LDH Nanosheet@Ni<sub>3</sub>S<sub>2</sub> Nanorod Hybrid Structures for Supercapacitor Electrode  
48  
49 Materials with Ultrahigh Specific Capacitance, *Sci. Rep.* 8 (2018) 5246.  
50  
51  
52  
53  
54  
55  
56  
57  
58  
59  
60  
61  
62  
63  
64  
65

- 1 [10] Z. Wang, P. Hong, S. Peng, T. Zou, Y. Yang, X. Xing, Z. Wang, R. Zhao, Z. Yan, Y. Wang,  
2  
3 Co(OH)<sub>2</sub>@FeCo<sub>2</sub>O<sub>4</sub> as Electrode Material for High Performance Faradaic Supercapacitor  
4  
5 Application, *Electrochim. Acta* 299 (2019) 312-319.  
6  
7  
8 [11] Y. Shao, M. F. El-Kady, J. Sun, Y. Li, Q. Zhang, M. Zhu, H. Wang, B. Dunn, R. B. Kaner,  
9  
10 Design and Mechanisms of Asymmetric Supercapacitors, *Chem. Rev.* 118 (2018) 9233-9280.  
11  
12 [12] X. Chu, H. Huang, H. Zhang, H. Zhang, B. Gu, H. Su, F. Liu, Y. Han, Z. Wang, N. Chen,  
13  
14 C. Yan, W. Deng, W. Deng, W. Yang, Electrochemically building three-dimensional  
15  
16 supramolecular polymer hydrogel for flexible solid-state micro-supercapacitors, *Electrochim.*  
17  
18 *Acta* 301 (2019) 136-144.  
19  
20  
21 [13] G. Luo, K. S. Teh, Y. Xia, Y. Luo, Z. Li, S. Wang, L. Zhao, Z. Jiang, A Novel Three-  
22  
23 Dimensional Spiral CoNi LDHs on Au@ErGO Wire for High Performance Fiber  
24  
25 Supercapacitor Electrodes, *Mater. Lett.* 236 (2019) 728-731.  
26  
27  
28 [14] C. Zhao, F. Ren, Yang Cao, X. Xue, X. Duan, H. Wang, L. Chang, Facile Synthesis of  
29  
30 Co(OH)<sub>2</sub>/Al(OH)<sub>3</sub> Nanosheets with Improved Electrochemical Properties for Asymmetric  
31  
32 Supercapacitor, *J. Phys. Chem. Solids* 112 (2018) 54-60.  
33  
34  
35 [15] Y. Lv, A. Liu, Z. Shi, J. Mu, Z. Guo, X. Zhang, H. Che, Hierarchical MnCo<sub>2</sub>O<sub>4</sub>/NiMn  
36  
37 Layered Double Hydroxide Composite Nanosheet Arrays on Nickel Foam for Enhanced  
38  
39 Electrochemical Storage in Supercapacitors, *ChemElectroChem* 5 (2018) 3968-3979.  
40  
41  
42 [16] X. Lu, C. Shen, Z. Zhang, E. Barrios, L. Zhai, Core-Shell Composite Fibers for High-  
43  
44 Performance Flexible Supercapacitor Electrodes, *ACS Appl. Mater. Interfaces* 10 (2018) 4041-  
45  
46 4049.  
47  
48  
49 [17] Y. Zhao, H. Dong, X. He, J. Yu, R. Chen, Q. Liu, J. Liu, H. Zhang, R. Li, J. Wang, Design  
50  
51  
52  
53  
54  
55  
56  
57  
58  
59  
60  
61  
62  
63  
64  
65

1 of 2D mesoporous Zn/Co-based metal-organic frameworks as a flexible electrode for energy  
2 storage and conversion, *J. Power Sources* 438 (2019) 227057.  
3

4  
5  
6 [18] T. Hao, W. Wang, D. Yu, Hierarchical NiCo Layered Double Hydroxides Nanosheets on  
7 Carbonized CNT/Cotton as a High-Performance Flexible Supercapacitor, *J. Mater. Sci.* 53  
8 (2018) 14485-14494.  
9

10  
11  
12 [19] Q. Yin, D. Li, J. Zhang, Y. Zhao, C. Wang, J. Han, CoNi-layered double hydroxide array  
13 on graphene-based fiber as a new electrode material for microsupercapacitor, *Appl. Surf. Sci.*  
14 487 (2019) 1-8.  
15  
16

17  
18  
19 [20] P. Bandyopadhyay, X. Li, N.H. Kim, J.H. Lee, Graphitic carbon nitride modified  
20 graphene/NiAl layered double hydroxide and 3D functionalized graphene for solid-state  
21 asymmetric supercapacitors, *Chem. Eng. J.* 353 (2018) 824-838.  
22

23  
24  
25 [21] L. Huang, B. Liu, H. Hou, L. Wu, X. Zhu, J. Hu, J. Yang, Facile Preparation of Flower-  
26 Like NiMn Layered Double Hydroxide/Reduced Graphene Oxide Microsphere Composite for  
27 High-Performance Asymmetric Supercapacitors, *J. Alloys Compds.*, 730 (2018) 71-80.  
28

29  
30  
31 [22] D.P. Dubal, N.R. Chodankar, R. Holze, D.H. Kim, P. Gomez-Romero, Ultrathin  
32 Mesoporous  $\text{RuCo}_2\text{O}_4$  Nanoflakes: An Advanced Electrode for High-Performance  
33 Asymmetric Supercapacitors, *ChemSusChem* 10 (2017) 1771-1782.  
34

35  
36  
37 [23] F. Su, M. Miao, Asymmetric carbon nanotube- $\text{MnO}_2$  two-ply yarn supercapacitors for  
38 wearable electronics, *Nanotechnology* 25 (2014) 135401.  
39

40  
41  
42 [24] H. Gao, F. Xiao, C.B. Ching, H. Duan, High-performance asymmetric supercapacitor  
43 based on graphene hydrogel and nanostructured  $\text{MnO}_2$ , *ACS Appl. Mater. Interfaces* 4 (2012)  
44 2801-2810.  
45  
46  
47  
48  
49  
50  
51  
52  
53  
54  
55  
56  
57  
58  
59  
60  
61  
62  
63  
64  
65

- 1 [25] Y. Zhang, M. Dong, S. Zhu, C. Liu, Z. Wen, MnO<sub>2</sub>@Colloid Carbon Spheres  
2  
3 Nanocomposites with Tunable Interior Architecture for Supercapacitors, Mater. Res. Bull. 49  
4  
5 (2014) 448-453.  
6  
7  
8  
9 [26] F. Li, H. Chen, X.Y. Liu, S.J. Zhu, J.Q. Jia, C.H. Xu, F. Dong, Z.Q. Wen, Y.X. Zhang,  
10  
11 Low-cost high-performance asymmetric supercapacitors based on Co<sub>2</sub>AlO<sub>4</sub>@MnO<sub>2</sub>  
12  
13 nanosheets and Fe<sub>3</sub>O<sub>4</sub> nanoflakes, J. Mater. Chem. A 4 (2016) 2096-2104.  
14  
15  
16  
17 [27] A. Tyagi, M. Chandra Joshi, K. Agarwal, B. Balasubramaniam, R.K. Gupta, Three-  
18  
19 dimensional nickel vanadium layered double hydroxide nanostructures grown on carbon cloth  
20  
21 for high-performance flexible supercapacitor applications, Nanoscale Adv. 1 (2019) 2400-2407.  
22  
23  
24  
25 [28] A. D. Jagadale, G. Guan, X. Li, X. Du, X. Ma, X. Hao, A. Abudula, Ultrathin Nanoflakes  
26  
27 of Cobalt-Manganese Layered Double Hydroxide with High Reversibility for Asymmetric  
28  
29 Supercapacitor, J. Power Sources 306 (2016) 526-534.  
30  
31  
32  
33 [29] S. Liu, S.C. Lee, U. Patil, I. Shackery, S. Kang, K. Zhang, J.H. Park, K.Y. Chung, S. Chan  
34  
35 Jun, Hierarchical MnCo-layered double hydroxides@Ni(OH)<sub>2</sub> core-shell heterostructures as  
36  
37 advanced electrodes for supercapacitors, J. Mater. Chem. A 5 (2017) 1043-1049.  
38  
39  
40  
41 [30] Y. Yang, L. Dang, M.J. Shearer, H. Sheng, W. Li, J. Chen, P. Xiao, Y. Zhang, R.J. Hamers,  
42  
43 S. Jin, Highly Active Trimetallic NiFeCr Layered Double Hydroxide Electrocatalysts for  
44  
45 Oxygen Evolution Reaction, Adv. Energy. Mater. 8 (2018) 1703189.  
46  
47  
48  
49 [31] X. Zang, C. Shen, E. Kao, R. Warren, R. Zhang, K. S. Teh, J. Zhong, M. Wei, B. Li, Y.  
50  
51 Chu, M. Sanghadasa, A. Schwartzberg, L. Lin, Titanium Disulfide Coated Carbon Nanotube  
52  
53 Hybrid Electrodes Enable High Energy Density Symmetric Pseudocapacitors, Adv. Mater. 30  
54  
55 (2018) 1704754.  
56  
57  
58  
59  
60  
61  
62  
63  
64  
65

- 1 [32] M. Li, R. Jijie, A. Barras, P. Roussel, S. Szunerits, R. Boukherroub, NiFe layered double  
2 hydroxide electrodeposited on Ni foam coated with reduced graphene oxide for high-  
3 performance supercapacitors, *Electrochim. Acta* 302 (2019) 1-9.  
4  
5  
6  
7  
8  
9 [33] A.D. Jagadale, G. Guan, X. Li, X. Du, X. Ma, X. Hao, A. Abudula, Ultrathin nanoflakes  
10 of cobalt–manganese layered double hydroxide with high reversibility for asymmetric  
11 supercapacitor, *J. Power Sources* 306 (2016) 526-534.  
12  
13  
14  
15  
16  
17 [34] Y.-P. Lin, N.-L. Wu, Characterization of  $\text{MnFe}_2\text{O}_4/\text{LiMn}_2\text{O}_4$  Aqueous Asymmetric  
18 Supercapacitor, *J. Power Sources* 196 (2011) 851-854.  
19  
20  
21  
22 [35] C. Tang, Z. Tang, H. Gong, Hierarchically Porous Ni-Co Oxide for High Reversibility  
23 Asymmetric Full-Cell Supercapacitors, *J. Electrochem. Soc.* 159 (2012) A651-A656.  
24  
25  
26  
27 [36] H. Luo, B. Wang, T. Liu, F. Jin, R. Liu, C. Xu, C. Wang, K. Ji, Y. Zhou, D. Wang, S. Dou,  
28 Hierarchical design of hollow Co-Ni LDH nanocages strung by  $\text{MnO}_2$  nanowire with enhanced  
29 pseudocapacitive properties, *Energy Storage Mater.* 19 (2019) 370-378.  
30  
31  
32  
33  
34  
35 [37] W. Huang, A. Zhang, X. Li, J. Tian, L. Yue, L. Cui, R. Zheng, D. Wei, J. Liu, Multilayer  
36 NiMn layered double hydroxide nanosheets covered porous  $\text{Co}_3\text{O}_4$  nanowire arrays with  
37 hierarchical structure for high-performance supercapacitors, *J. Power Sources* 440 (2019)  
38 227123.  
39  
40  
41  
42  
43  
44  
45  
46 [38] X. Guan, M. Huang, L. Yang, G. Wang, X. Guan, Facial design and synthesis of  $\text{CoS}_x/\text{Ni}$ -  
47 Co LDH nanocages with rhombic dodecahedral structure for high-performance asymmetric  
48 supercapacitors, *Chem. Eng. J.* 372 (2019) 151-162.  
49  
50  
51  
52  
53  
54  
55  
56  
57  
58  
59  
60  
61  
62  
63  
64  
65